

Earth-based 12.6-cm wavelength radar mapping of the Moon: New views of impact melt distribution and mare physical properties

Bruce A. Campbell^{a,*}, Lynn M. Carter^a, Donald B. Campbell^b, Michael Nolan^c, John Chandler^d, Rebecca R. Ghent^e, B. Ray Hawke^f, Ross F. Anderson^a, Cassandra Wells^b

^a Center for Earth and Planetary Studies, Smithsonian Institution, MRC 315, PO Box 37012, Washington, DC 20013-7012, USA

^b National Astronomy and Ionosphere Center, Cornell University, Ithaca, NY 14853, USA

^c Arecibo Observatory, HCO3 Box 53995, Arecibo, PR 00612, USA

^d Smithsonian Astrophysical Observatory, 60 Garden St., Cambridge, MA 02138, USA

^e Department of Geology, University of Toronto, Toronto, Canada

^f HIGP, University of Hawaii, 1680 East–West Road, Honolulu, HI 96822, USA

ARTICLE INFO

Article history:

Received 2 December 2009

Revised 27 February 2010

Accepted 11 March 2010

Available online 16 March 2010

Keywords:

Moon

Volcanism

Impact processes

ABSTRACT

We present results of a campaign to map much of the Moon's near side using the 12.6-cm radar transmitter at Arecibo Observatory and receivers at the Green Bank Telescope. These data have a single-look spatial resolution of about 40 m, with final maps averaged to an 80-m, four-look product to reduce image speckle. Focused processing is used to obtain this high spatial resolution over the entire region illuminated by the Arecibo beam. The transmitted signal is circularly polarized, and we receive reflections in both senses of circular polarization; measurements of receiver thermal noise during periods with no lunar echoes allow well-calibrated estimates of the circular polarization ratio (CPR) and the four-element Stokes vector. Radiometric calibration to values of the backscatter coefficient is ongoing. Radar backscatter data for the Moon provide information on regolith dielectric and physical properties, with particular sensitivity to ilmenite content and surface or buried rocks with diameter of about one-tenth the radar wavelength and larger.

Average 12.6-cm circular polarization ratio (CPR) values for low- to moderate-TiO₂ mare basalt deposits are similar to those of rough terrestrial lava flows. We attribute these high values to abundant few-centimeter diameter rocks from small impacts and a significant component of subsurface volume scattering. An outflow deposit, inferred to be impact melt, from Glushko crater has CPR values near unity at 12.6-cm and 70-cm wavelengths and thus a very rugged near-surface structure at the decimeter to meter scale. This deposit does not show radar-brightness variations consistent with levees or channels, and appears to nearly overtop a massif, suggesting very rapid emplacement. Deposits of similar morphology and/or radar brightness are noted for craters such as Pythagoras, Rutherford, Theophilus, and Aristillus. Images of the north pole show that, despite recording the deposition of Orientale material, Byrd and Peary craters do not have dense patterns of radar-bright ejecta from small craters on their floors. Such patterns in Amundsen crater, near the south pole, were interpreted as diagnostic of abundant impact melt, so the fraction of Orientale-derived melt in the north polar smooth plains, 1000 km farther from the basin center, is inferred to be much lower.

Published by Elsevier Inc.

1. Introduction

Radar remote sensing has long been used to study the physical properties of the lunar regolith. Early work at Arecibo and Haystack Observatory provided almost full nearside coverage at 7.5-m, 70-cm, and 3.8-cm wavelength, with spatial resolution of 20–40 km, 2–5 km, and 2 km respectively (Thompson, 1978, 1987; Zisk et al., 1974). More recently, we obtained a 70-cm nearside map with spatial resolution as fine as 450 m per pixel, using fo-

cused processing techniques (e.g., Stacy, 1993) to obtain this resolution over the entire illuminated region (Campbell et al., 2007). The 12.6-cm (S-band) Arecibo radar system was used for observations of shadowed regions at the poles and demonstrations of focused processing (Stacy et al., 1997). A major reason for not mapping large areas was the requirement to receive 12.6-cm echoes from the Moon at a secondary antenna, since the ~2.5 s light travel time does not provide a safe margin of transmitter power ramp-down for operation of the receivers.

The secondary antenna at Arecibo used in earlier studies is no longer available, but the commissioning of the Green Bank Telescope (GBT) in 2001 made it possible to carry out dual-polarization,

* Corresponding author.

E-mail address: campbellb@si.edu (B.A. Campbell).

bistatic mapping with relative ease. Image resolution as fine as 20 m per pixel has been achieved (Campbell et al., 2006), and these results suggested that synoptic mapping would be of value for studies of lunar geology, resource potential, and landing site hazards. Coverage of large areas, with the capability to produce Stokes-polarimetry products, at 12.6-cm wavelength provides regional context for images collected by radar systems on Chandrayaan-1 and the Lunar Reconnaissance Orbiter. Our basic data have a single-look horizontal spatial resolution of 40 m per pixel, and are averaged to an 80-m resolution, four-look image to reduce speckle noise.

We describe in Section 2 the S-band observing, mapping, and calibration techniques. Section 3 analyzes the radar polarization properties of basaltic deposits as an initial step in improving techniques for age-dating small patches of mare material. Section 4 presents new insights on the distribution and surface morphology of impact melt deposits from the crater to basin scale.

2. Radar mapping and calibration

Radar images of the lunar surface are produced using the delay-Doppler technique (e.g., Thompson and Dyce, 1966; Pettengill et al., 1974), which forms a coordinate system based on the round-trip time variations in the echoes and their frequency shift with respect to a chosen target location. The region of the Moon amenable to such mapping varies with libration, which brings different parts of the limb into view. The horizontal spatial resolution along the range direction is dictated by the delay resolution of the transmitted signal and the radar incidence angle at a point on the Moon's surface. For regions close to the apparent spin axis, lines of constant frequency offset are roughly orthogonal to the axis of increasing delay, and the horizontal spatial resolution with Doppler shift is defined by the apparent spin rate of the Moon and the duration of the coherent observation period. A region at the center of the nearside cannot be mapped due to the coarse ground resolution along the delay axis and the high degree of north-south ambiguity when pointing the radar close to the sub-Earth location.

We transmit a circularly polarized, continuous-wave (CW) signal at 12.6-cm wavelength from Arecibo. This signal is modulated by a 65535-sample pseudo-random noise (PN) code with baud length of 0.2 μ s. The resulting inter-pulse period of 13.107 ms allows for a window within each pulse record that samples only the receiver thermal noise. The coherence interval, or length of each observation, is 1718 s, which provides about a 40-m spatial resolution along the frequency axis. We receive the echoes from the Moon at the GBT in both senses of circular polarization, using 4-bit analog-to-digital conversion to quadrature sample the voltages at 5 MHz rate through a 4.4-MHz Gaussian lowpass filter. Circular-polarized echoes in the opposite sense as that transmitted (OC or "polarized") arise in part from mirror-like scattering features, with some component due to diffuse reflections, while echoes in the same sense as that transmitted (SC or "depolarized") arise solely due to double-bounce or diffuse scattering.

Initial processing correlates the signals with the PN code, then averages every four pulses to increase signal-to-noise and reduce data volume. Focused image formation and mapping to a latitude-longitude format follows the steps described for the 70-cm data by Campbell et al. (2007). The principal steps in this processing are: (1) determination (from a polynomial representation of the sub-radar point location, apparent lunar spin rate, and axial tilt with time) of a delay and frequency history for the center of any chosen small patch within the illuminated region, (2) range migration and phase rotation of the raw data to match this history, and (3) Fourier-transform mapping of the image power and coordinate transformation to a latitude-longitude grid. The output image is a

checkerboard of such focused patches, which are small enough (typically 5×5 km) to avoid defocusing over the coherence interval. The delay and frequency resolution are chosen to provide about 40-m horizontal spatial resolution in both dimensions, and we average by two along both axes to derive a four-look power image with 80-m sampling. These images, along with circular polarization ratio (CPR) values based on 100-look (400 m resolution)

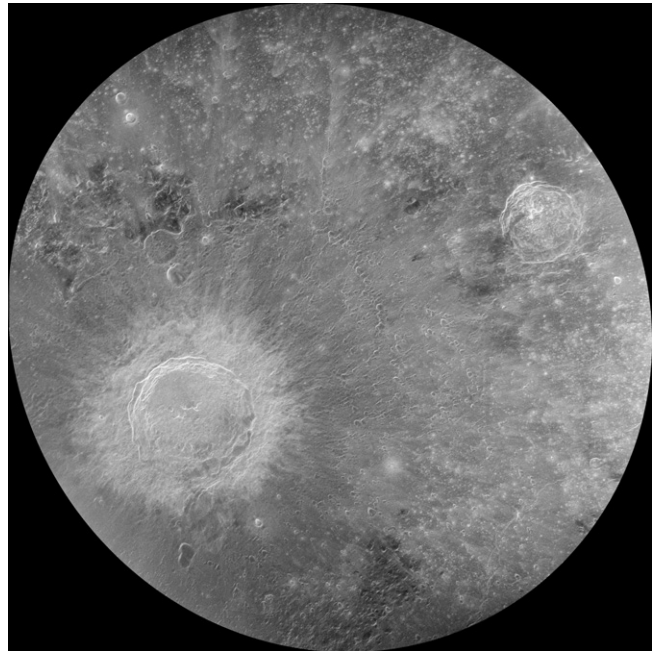


Fig. 1. S-band same-sense circular (SC) polarization radar image of Copernicus crater (93 km diameter, 9.7°N, 20.0°W) and northeastern portion of its distal ejecta deposits. Note the strong radar returns from the crater floor, attributed to very rugged deposits of fractured impact melt. Image representative of PDS-deliverable products, with pointing errors corrected, beam pattern changes in brightness minimized, and edges truncated at the -22 dB point of the net Arecibo-GBT beam pattern.

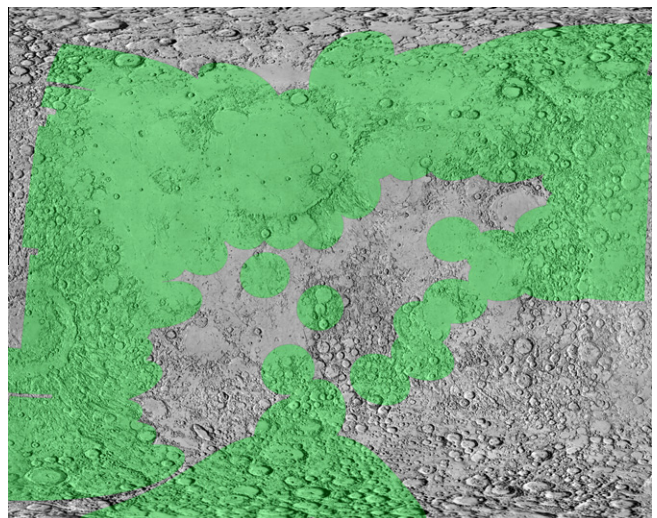


Fig. 2. Map of Earth-based 12.6-cm wavelength non-polar radar image coverage through January 2010, shown as green highlighting on USGS shaded-relief map. Image area 80°S–80°N, 100°E–100°W, simple cylindrical projection. Coverage represents areas out to the -15 dB point of the net Arecibo-GBT beam pattern.

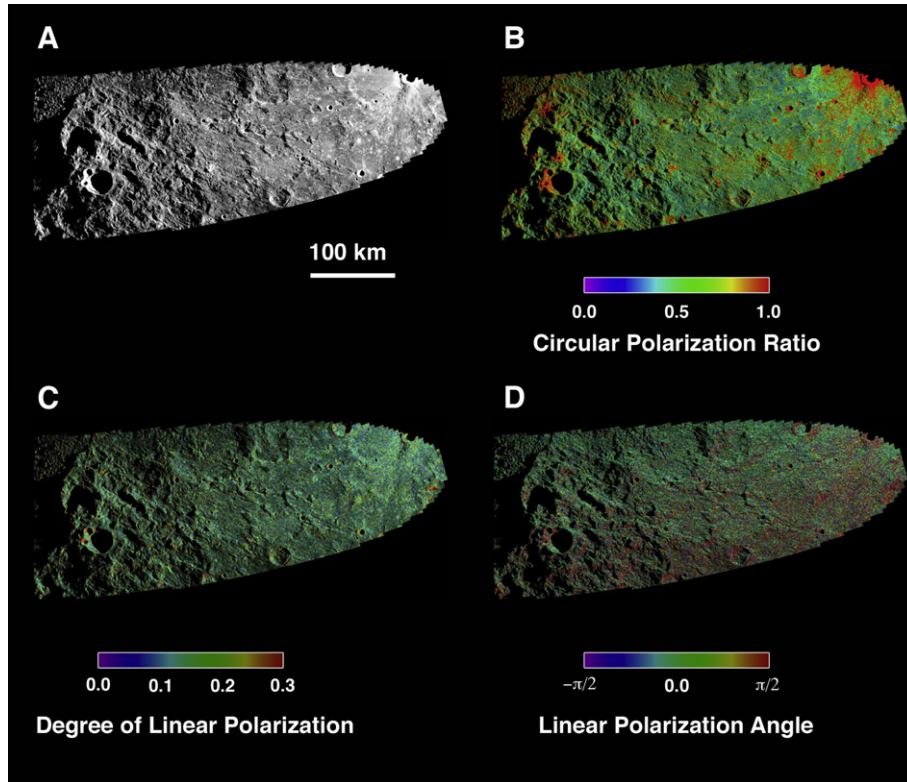


Fig. 3. Example of (A) 12.6 cm radar image, (B) circular polarization ratio, (C) degree of linear polarization (DLP), and (D) linear polarization angle for a region on the southwestern Montes Cordillera deposits of Orientale Basin. The circular crater at lower left is Krasnov (29.9°S, 79.6°W). The radar-bright crater with high CPR (abundant surface and subsurface rocks 2 cm in diameter and larger) deposits at upper right is Byrgius A. The linear polarization angle is dominated by local tilts along the axis (roughly N–S here) perpendicular to the radar look direction. The DLP is modulated by the relative roles of surface and subsurface scattering, with high values suggesting a strong subsurface reflection.

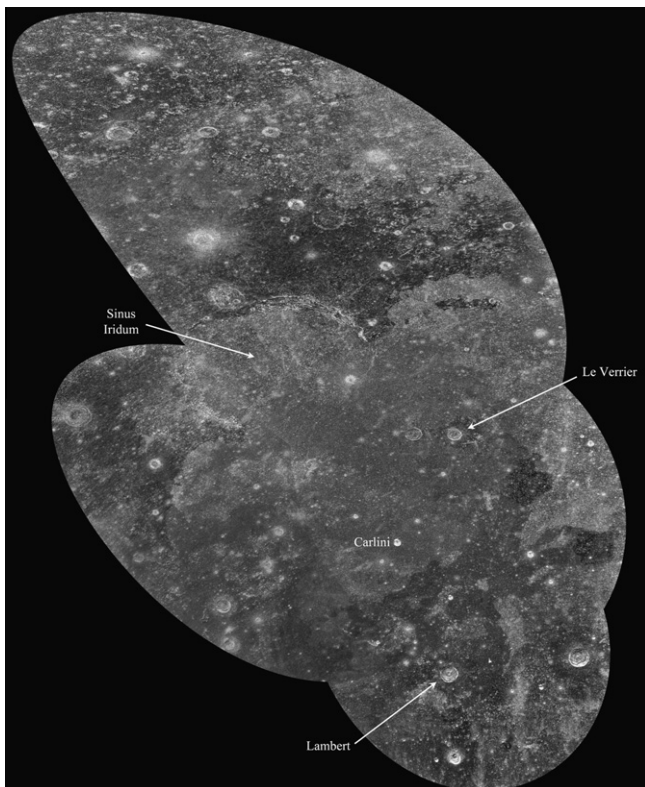


Fig. 4. Mosaic of circular polarization ratio data from four separate Arecibo–GBT observations at 12.6-cm wavelength for Mare Imbrium. Range of contrast values corresponds to $\mu_c = 0$ –2. Bounds of radar-imaged areas 18.8–46.1°N, 10.4–45.1°W.

averaging, will be delivered to the Planetary Data System (PDS) for archiving and distribution.

During the mapping, the power in each pixel is normalized to the contributing surface area as the first step in deriving calibrated values of the dimensionless backscatter coefficient, σ^0 . We also divide by the average noise power measured during the portion of the inter-pulse period when no echoes from the Moon are present. The remaining factors in determining the backscatter coefficient are the respective antenna gains (73 dB for Arecibo and 66.4 dB for GBT at 12.6 cm), the average transmitted power as measured at Arecibo (typically 40–60 kW), and the absolute system temperature corresponding to the receiver noise for any given GBT pointing location on the Moon (Campbell et al., 2007).

We determined the 12.6-cm GBT system temperature, T_{sys} , as a function of the angular offset of the pointing target from the center of the Moon (analogous to the radar incidence angle, ϕ). The temperature, in degrees Kelvin, when pointed at the center of the lunar disk was determined by reference to a flux calibrator of known brightness (the quasar 3C48), and the angular variation was derived by a fit to measurements over a range of beam locations:

$$T_{\text{sys}} = 268 + 0.01\phi - 0.019\phi^2 \quad (1)$$

The estimated system temperature when the relatively narrow GBT beam is pointed at the center of the Moon is, as expected, higher than typical values obtained with a wider beam that includes the lunar limbs (Hagfors, 1970; Keihm and Langseth, 1975).

We also compensate for the variation in the combined beam pattern power gain with angular distance from a pointing location, κ , represented by a first-order Bessel function with an “effective width” parameter, W , of 700:

$$P(\kappa) = [J_1(2W\pi \sin \kappa)/(W\pi \sin \kappa)]^4 \quad (2)$$

This pattern has its first null near a beam angle of 0.05° . The actual location on the Moon of the beam center often differs from that specified, reflecting the inherent pointing accuracy of the Arecibo antenna. We determine the “true” latitude and longitude of the beam center through a simple iterative process that matches an ideal beam pattern to the location of the first nulls in the radar map. The final image products for each observation are then corrected for the variation in gain (Eq. (2)) with respect to the best-fit pointing center and trimmed to the region where the beam is within -22 dB (a beam angle of 0.037°) of its maximum value (Fig. 1). CPR values are typically reliable to about the -15 dB point in the beam pattern. For the PDS, we will also provide images that have been normalized to a $\cos \phi$ scattering law, which removes much of the variability in brightness due to changes in viewing geometry (especially in the SC maps).

With these corrections, we obtain images that typically mosaic with only 1–2 dB in brightness variations, with very good calibration between the SC and OC channels for analysis of CPR (SC/OC) variations. Coverage of the nearside and limb regions through January 2010 is shown in Fig. 2. To date, our calculated values of σ^0 , while consistent within a narrow range across the various observing runs, remain a factor of 8–10 lower than expected based on full-disk scattering measurements documented by Hagfors (1970). One possible reason for this offset is aliasing of system noise into the sampled data.

We can also produce from the complex-valued dual-polarization data estimates of the four Stokes vector elements, and thus values for the degree of linear polarization (DLP) and polarization angle χ (Fig. 3). Taken together, the backscatter coefficient, CPR, DLP, and χ provide a more complete view of the dominant scattering mechanisms and relative strengths of surface versus subsurface echoes. The importance of such information for geologic interpretation has been well demonstrated for Venus (e.g., Carter et al., 2004, 2006), but only in relatively limited applications to date for the Moon (Campbell et al., 1992; Stacy, 1993). Our new data, and dual-polarization sensors on the LRO and Chandrayaan-1 spacecraft, will make it possible to study large areas of the Moon with this technique.

3. Radar polarimetric properties of the maria

The lunar maria exhibit substantial variability in age and composition. Differences in the abundance of the mineral ilmenite (FeTiO_3) strongly affect UV–Visible reflectance properties (e.g., Charette et al., 1974; Lucey et al., 2000), and play a major role in modulating the same-sense circular (SC) diffuse radar echoes (and the CPR) through changes in the loss tangent of the regolith (Carrier et al., 1991; Schaber et al., 1975; Campbell et al., 1997). Mare age variations (e.g., Hiesinger et al., 2000) control primarily the thickness and rock abundance of the regolith, with younger flows having thinner, more rocky deposits than older terrain. These differences are most evident in thermal infrared images (e.g., Shorthill, 1973), and appear to modulate the SC radar echo to an increasing degree with shorter wavelength (Campbell et al., 2009b). The S-band backscatter data, in conjunction with UV–VIS estimates of TiO_2 content, may thus provide a tool for discriminating variations in age among mare units too small for crater-count statistics. The first step in developing this technique is to determine the average behavior for a large sample of the maria.

Our new S-band data cover large mare regions, permitting a robust estimate of the variability in circular polarization ratio as a function of incidence angle and the basalt TiO_2 content inferred from modeling of Clementine UV–VIS data (Gillis et al., 2003). Potential variations in radar echoes due to age differences among the

mare units are not considered in this first-order analysis. Fig. 4 shows a CPR map of Mare Imbrium assembled from four Arecibo–GBT observations; the relative channel calibration applied to individual runs clearly yields consistent results. Fig. 5 shows the mean behavior of the 12.6-cm CPR with titanium content at 35 – 55° incidence angles for this region. The dashed line in this figure denotes the best-fit functional dependence of 70-cm echoes for the same geometry (Campbell et al., 2009b). The large offset between 12.6-cm and 70-cm values is not unexpected; Hagfors (1970, Fig. 23) shows that the disk-integrated CPR for 68-cm wavelength reaches a maximum of about 0.4–0.5 toward the limb (grazing incidence), while 23-cm echoes reach a maximum CPR of 0.5–0.6, with the asymptotic behavior occurring at smaller incidence angles for shorter wavelength.

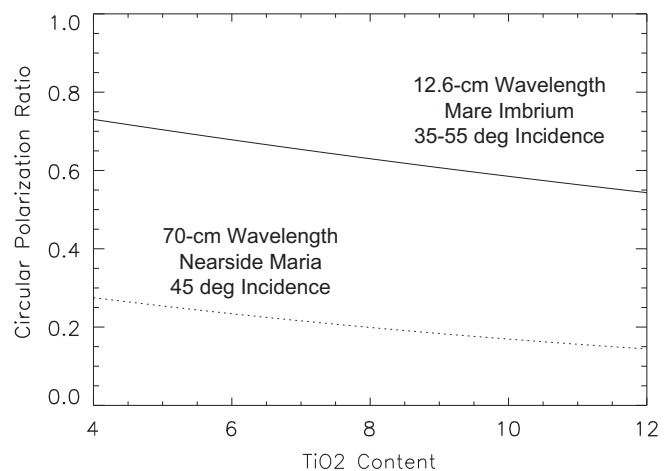


Fig. 5. Circular polarization ratio at 12.6-cm wavelength (solid line) as a function of UV–VIS derived TiO_2 abundance (in percent), based on fit to Mare Imbrium data for incidence angles of 35 – 55° . Dashed line is mean behavior of the nearside maria at 70-cm wavelength for 45° incidence angle (Campbell et al., 2009a).

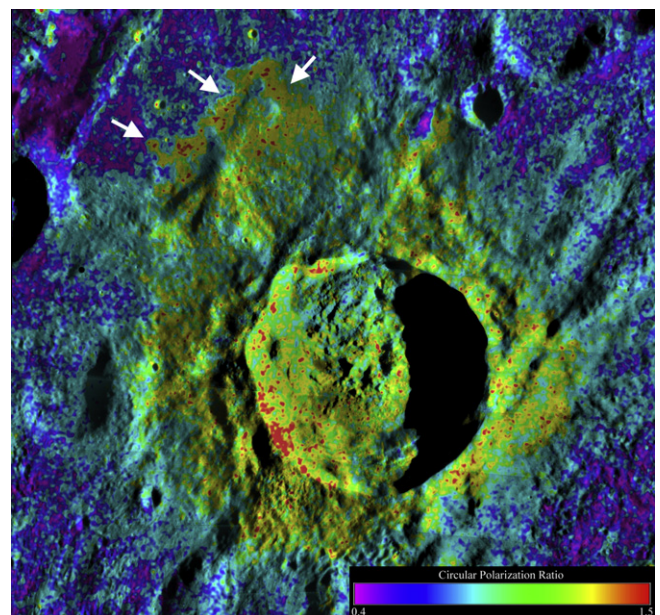


Fig. 6. Lunar Orbiter IV image of Glushko crater (8.4°N , 77.6°W , 43 km diameter), with color overlay of 12.6-cm circular polarization ratio values. Note the high CPR values (orange and red tones) in the northern outflow deposit indicated by white arrows.

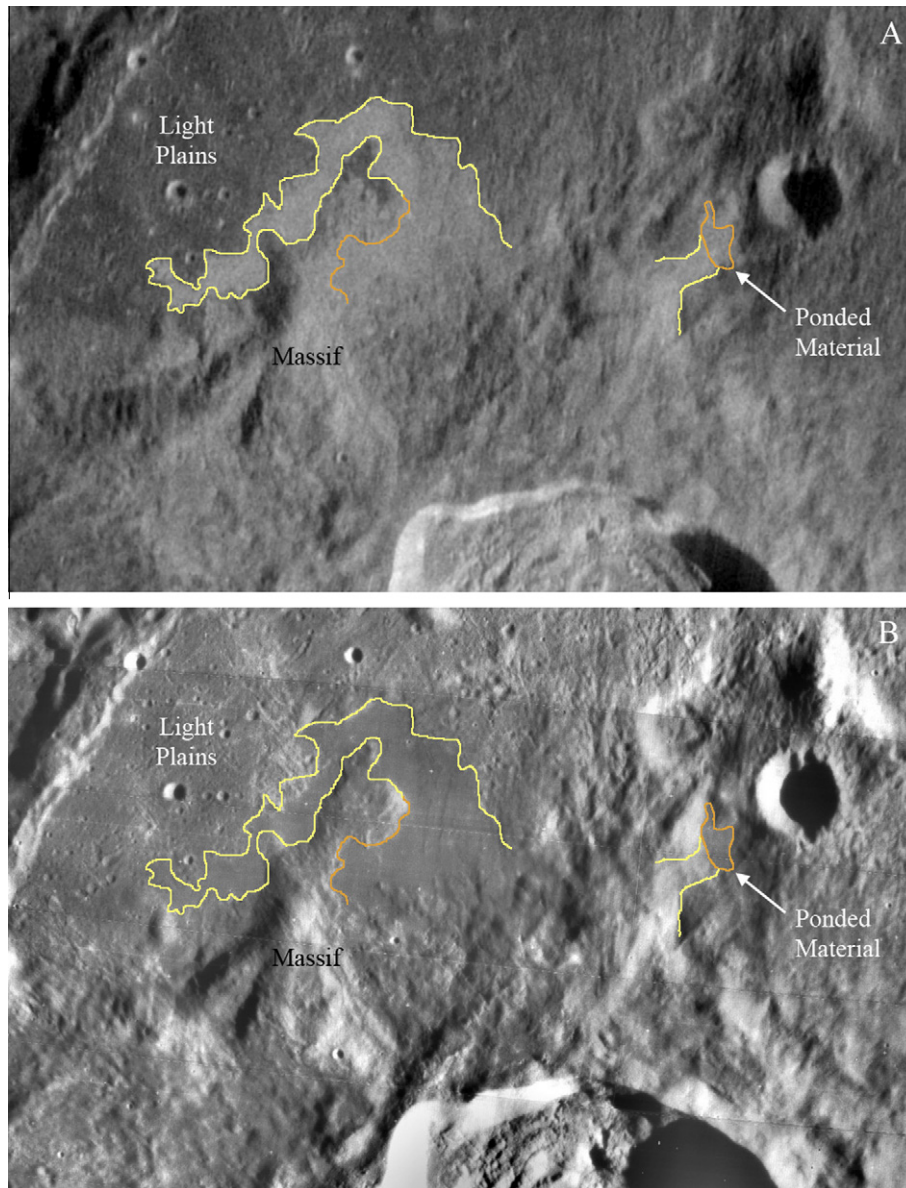


Fig. 7. (A) 12.6-cm wavelength, same-sense circular polarization (SC) radar image of Glushko crater (43 km diameter) northern rim and ejecta deposits. Image width 80 km. Yellow outlines indicate bounds of rough, radar-bright flows delineated from radar image; orange outlines show limits inferred from smooth regions in photographic data; (B) Lunar Orbiter IV image of identical region. Note the partial overtopping of the north-trending massif at left center by radar-bright material.

The mean circular polarization ratios for Mare Imbrium flows of low TiO_2 content are similar to or greater than those of rough terrestrial lava surfaces, which have a maximum CPR value of about 0.6 at 60° incidence angle (Campbell, 2009). These relatively high values are partly a result of the sensitivity of the 12.6-cm radar signal to few-centimeter scale, near-surface rocks associated with even small impact craters in the mare regolith. Such small debris is not a strong contributor to the 70-cm echoes. As a result, the overall trend of diminishing diffuse echoes with increasing loss tangent (greater TiO_2 content) is superposed on a higher “background” CPR value due to the much larger population of wavelength-scale scatterers. Due to the long tail of crater-related high values, the CPR within any sample area follows a Rayleigh distribution, so the most common value (the mode rather than the mean) is about 80% of that shown by the best-fit function.

Diffuse scattering from rocks suspended in the fine-grained regolith matrix will also contribute to the enhanced CPR, and has long been suggested to explain the generally higher backscatter cross

sections than predicted by surface rocks alone (e.g., Thompson et al., 1970). The coherent backscattering effect, if it plays a role, strongly favors same-sense circular echoes over opposite-sense returns (Black et al., 2001), and may thus bias the CPR (SC/OC) upwards. The low efficiency of this mechanism for the lunar regolith (as opposed to voids in ice), requiring a least two bounces between rocks with modest reflectivity contrast, may limit its contribution to only those situations where surface rock faces form the proper double-bounce geometry.

4. Radar mapping of impact melt deposits

The impact process creates a large volume of comminuted debris that forms the proximal and distal ejecta blankets of a crater, and a smaller volume of melted material that is generally confined to the crater cavity. Ponded patches or lobate deposits within the ejecta blanket, sometimes with arcuate ridges that define a flow direction, appear to represent melt-rich material that escaped the

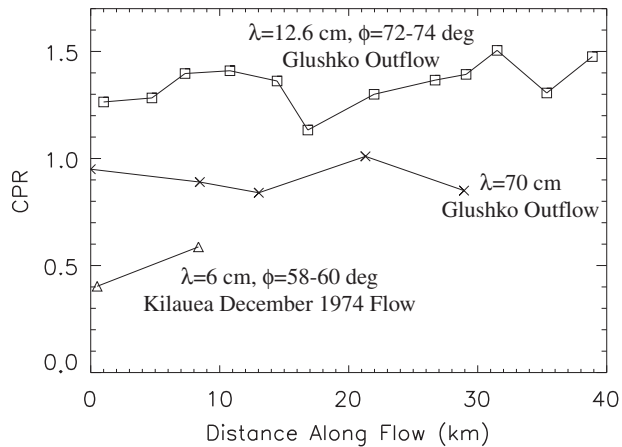


Fig. 8. Circular polarization ratio, at 12.6-cm and 70-cm wavelengths, versus distance from the outer margin of the continuous ejecta for the Glushko crater outflow deposit. For comparison, CPR values at 6-cm wavelength for the pahoehoe/aa transition in the December 1974 Kilauea lava flow are also plotted. The 70-cm CPR data are limited by the image resolution to cover only the wider, proximal portions of the Glushko outflow.

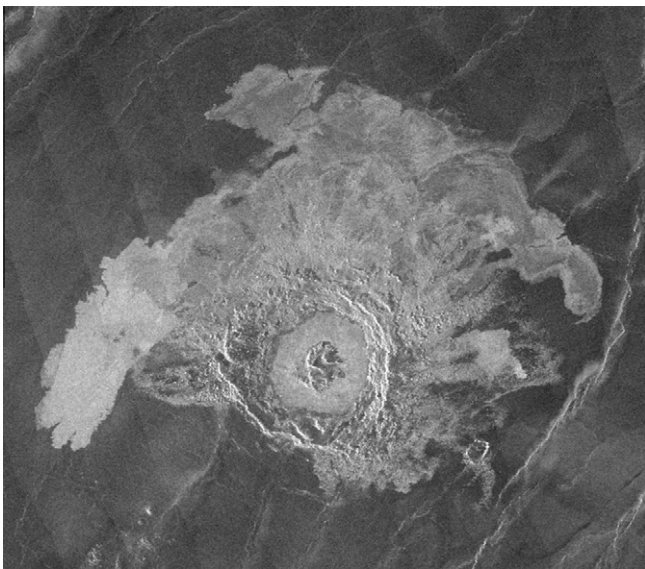


Fig. 9. Magellan image of lava-like outflows from crater Guan Daosheng (43 km diameter, 61.1°S, 181.8°E) on Venus.

central cavity (e.g., Hawke and Head, 1977; Heather and Dunkin, 2003). Larger instances of melt flows exterior to craters are relatively rare, in part due to the small percentage of extremely oblique impacts that preferentially distribute material outside the central cavity, and perhaps to the lack of distinguishing features in moderate-resolution optical images. We discuss below radar observations of lava-like flow features associated with numerous larger (>40 km diameter) craters, and a comparison of substantial differences in the occurrence of basin-derived melt material between the lunar north and south poles.

4.1. Young crater deposits

Younger crater floors have exceptionally bright SC radar returns (Fig. 1) and high CPR values due to the cracked and jumbled surface produced during flow and cooling of the melt sheets. Our new

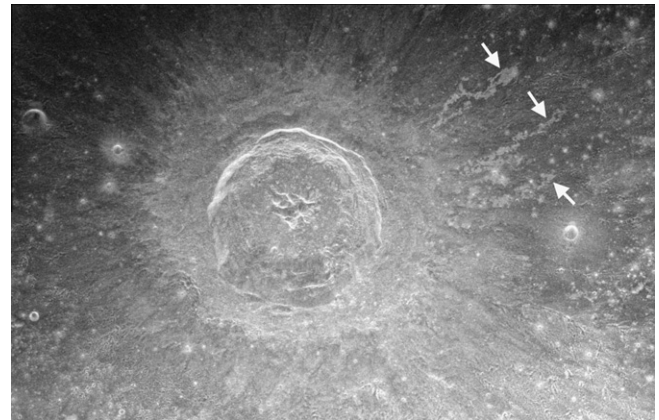


Fig. 10. S-band same-sense circular polarization radar image of Aristillus crater (55 km diameter, 33.9°N, 1.2°E). North at top. Note the lava-like flows, noted by arrows, extending about 65 km northeast and east from the crater rim.

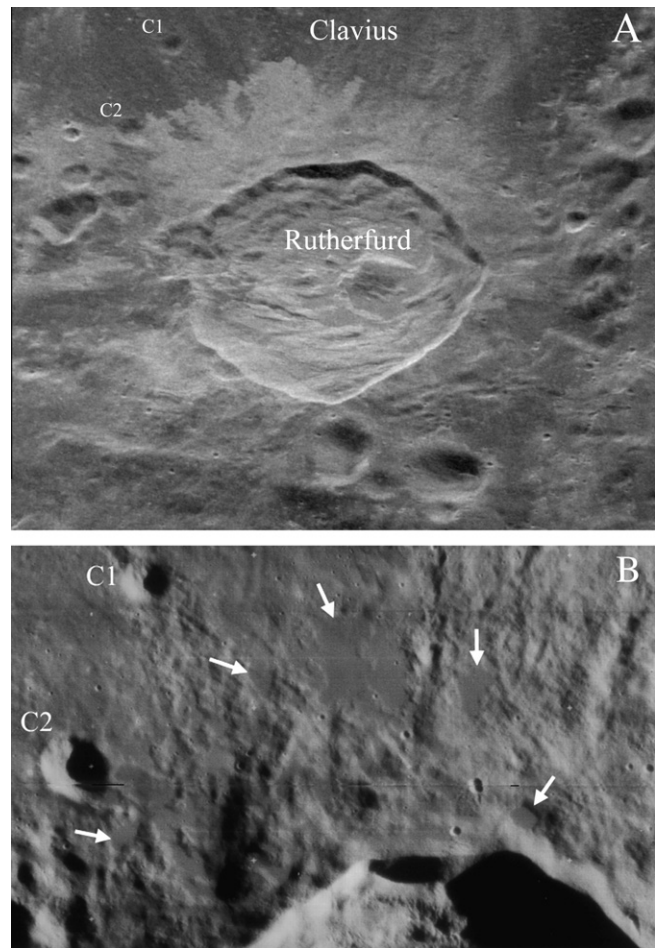


Fig. 11. (A) S-band same-sense circular polarization radar image of Rutherford crater (58 km diameter, 60.9°S, 12.1°W). Note the high-backscatter, lobate deposits on the floor of Clavius crater to the north. (B) Lunar Orbiter (part of frame IV-118-H3) view of the northern rim and ejecta deposits of Rutherford, with arrows noting smooth ponds of impact melt. Two small craters are labeled C1 and C2 as a location guide for this image within (A).

12.6-cm image data, and 70-cm coverage in areas not yet mapped at S-band, reveal contiguous, lava-like flows in the distal deposits of several craters, suggesting that such deposits may be more common, but under-recognized, for younger impacts. The deposits of

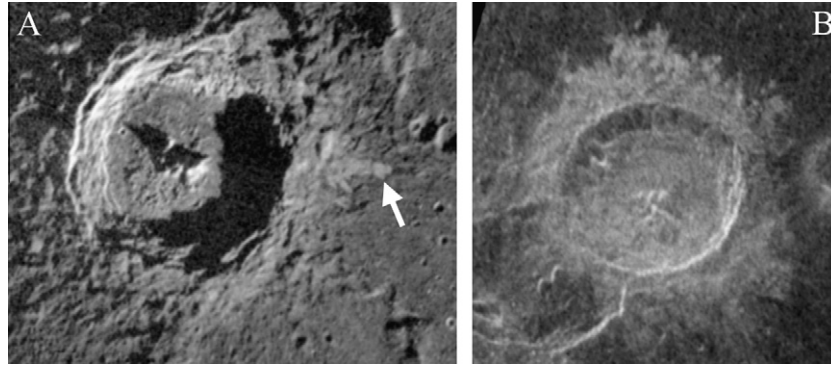


Fig. 12. 70-cm wavelength, same-sense circular polarization radar images of craters with potential impact melt deposits. (A) Pythagoras (63.5N, 63.0W, 142 km diameter), (B) Theophilus (11.4S, 26.4E, 110 km diameter). Pythagoras has a narrow, radar-bright distal deposit that may be a chain of melt ponds, shown by arrow. Lobate deposits of Theophilus appear to be similar to those of Rutherford (Fig. 11) in being preferentially distributed to one side (north of the crater).

Glushko crater (43 km diameter) are particularly striking (Fig. 6). The northern ejecta of this crater was identified as a thermal high by Schultz and Mendell (1978), suggesting rugged terrain, and the radar data clearly show a lobate, high-backscatter deposit winding about 40 km north and west from the edge of the continuous ejecta blanket (Fig. 7A). The high radar backscatter region corresponds with a very smooth surface at the tens of meter scale revealed by Lunar Orbiter IV photographs (Fig. 7B), and the radar makes clearer the distal extent of the flow deposit. A second flow lobe and associated pond are tentatively identified to the north-northeast of the crater. The high radar backscatter signature that begins at the margin of the ejecta blanket extends partially across the relatively flat top of a massif that diverts the flow, suggesting that the material was moving quickly enough to almost overtop the obstacle.

In the absence of absolute values for the backscatter coefficient, the circular polarization ratio provides our most robust measure of roughness (or block abundance) at the lunar surface or within the meter-scale probing depth of the 12.6-cm signal. In the terrae surrounding the crater, CPR values range from 0.65 to 0.70 for incidence angles of 72–74°. On the lobate, radar-bright deposit at similar angles, 12.6-cm CPR values range from 1.2 to 1.5. Variations in CPR along the length of this outflow deposit (Fig. 8) are relatively small, with no evidence for changes in morphology and radar properties analogous to the pahoehoe/aa transition in some terrestrial basalt flows. The CPR values remain high at 70-cm wavelength (Fig. 8), again with no significant variability over the length of the deposit. At both wavelengths, the northern continuous ejecta blanket of Glushko has lower CPR values than the outflow deposit (Fig. 6), suggesting that the melt largely drained away from the near-rim area.

Even allowing for the potentially high “background” CPR (Fig. 5), values of unity or larger are generally linked with very rugged lava flows or blocky deposits (Campbell et al., 2009a). The CPR drops by only about 10% with a fivefold increase in wavelength to the 70-cm values, so a very rough surface structure must persist over the decimeter to meter scale, buried by no more than about a meter of regolith. Maximum 12.6-cm CPR values for inferred melt deposits within Glushko are about 1.2, similar to those observed in the exterior outflow, but there are substantial variations across the crater floor (Fig. 6). The lack of obvious channel or levee structures (typical of many rugged terrestrial lava flows) in either the photographic or radar data, the homogenous radar polarization properties along its length, and the evidence for the flow material having nearly overtopped the massif, are all consistent with very rapid emplacement of this deposit.

Radar-bright crater outflow deposits are common for craters of this size range on Venus (Fig. 9), due in part to higher ambient temperatures (Chadwick and Schaber, 1993). The 12.6-cm backscatter

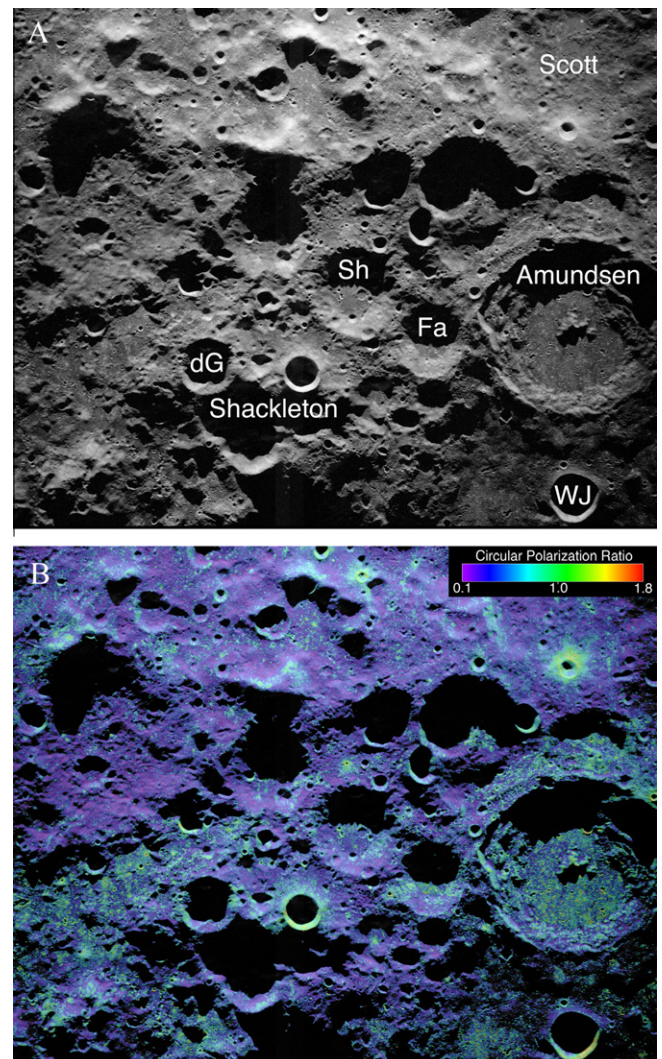


Fig. 13. (A) S-band opposite-sense circular (OC) radar backscatter image of the south polar region of the Moon. Polar stereographic projection; image resolution averaged to 160 m per pixel. Image width about 390 km. Zero longitude is toward top center. (B) Backscatter image with circular polarization ratio as color overlay. Note the streaks and patches of high CPR associated with small craters in the highlands west of de Gerlache (dG) and in the floors of craters Amundsen and Faustini (Fa).

coefficients of venusian outflows (there are no high-resolution CPR measurements) lie between typical σ^0 values for terrestrial aa and

pahoehoe lava morphologies (Johnson and Baker, 1994), which also exhibit CPR values well below unity (Fig. 8). The high CPR values of the Glushko impact melt (1.2–1.5) therefore suggest a more rugged surface texture, due either to intrinsic aspects of lunar melt rheology and/or cooling patterns or to a greater degree of erosion or mantling for the Venus deposits.

Exterior radar-bright flow-like features are also seen at the lunar craters Aristillus (55 km diameter), where they extend about 65 km from the rim (Fig. 10), and north of Rutherford (48 km diameter) where they are associated with both proximal hummocky ejecta and numerous ponded deposits observed in Lunar Orbiter

images (Fig. 11). Several other large craters, some mapped thus far only at 70-cm wavelength, also appear to have either narrow or apron-like features, possibly comprising multiple discrete melt ponds (Fig. 12). It seems likely that similar deposits occur at most younger craters but are obscured by or mixed with proximal ejecta, and are more noticeable for the above examples due to longer run-outs arising from extremely oblique impacts (Howard and Wilshire, 1975; Hawke and Head, 1977; Gault and Wedekind, 1978).

4.2. Basin-derived deposits near the poles

Impact melt deposits appear to extend to great distances for basin-scale events, as shown by 70-cm mapping of radar-bright, high CPR small crater clusters in smooth areas mapped as Imbrian-period plains units across the south polar region (Campbell and Campbell, 2006; Ghent et al., 2008). The enhanced radar backscatter from these small craters, attributed to a dense regolith substrate with cooled impact melt from Orientale, were revealed in greater detail by 12.6-cm images of the south pole (Fig. 13) (Campbell et al., 2006). Favorable libration for viewing the lunar north pole from Arecibo, which had been very limited in the past several years, occurred again in 2009, so we now have a comparison image showing the polarization properties of this area, 1000 km more distal to the center of Orientale (Fig. 14).

The craters Peary (73 km diameter) and Byrd (93 km diameter) are filled by smooth plains units (Luchitta, 1978), but the Peary floor appears to have many more craters in the 2–4 km diameter range (Fig. 14A). A count of all craters with diameter >1.2 km within Byrd and Peary shows that their cumulative frequency functions have very similar intercepts at the 1-km scale, implying ages of 3.86 and 3.88 byr (Fig. 15). Both crater floor deposits thus record materials of the Orientale impact around 3.85 byr, and were not resurfaced by mare flooding at some later date. We attribute the shallower cumulative crater-density slope for Peary (about -2 , in contrast to a value of -2.5 for Byrd) to a cluster of 2–4 km diameter Orientale secondary craters.

Despite the preserved record of Orientale ejecta within the north-polar crater floors, we do not observe the dense patterns of high CPR, radar-bright small craters that are so evident, for example, in Amundsen crater (74 km diameter) (Fig. 13B). This suggests that the large volume fraction of Orientale-derived melt inferred

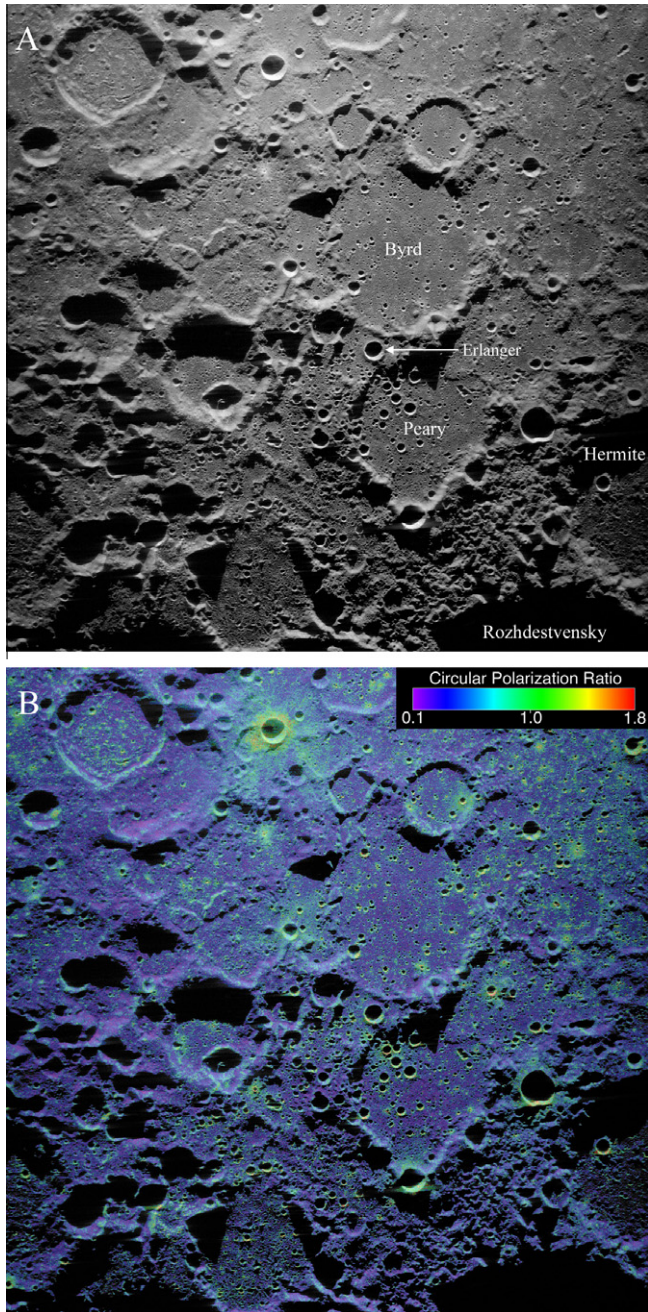


Fig. 14. (A) S-band opposite-sense circular (OC) radar backscatter image of the north polar region of the Moon. Polar stereographic projection; image width 365 km. Zero longitude toward top center. Note the cluster of 2–4 km diameter craters, attributed here to Orientale secondary impacts, between the center of Peary and the crater Erlanger. (B) Backscatter image with circular polarization ratio as color overlay.

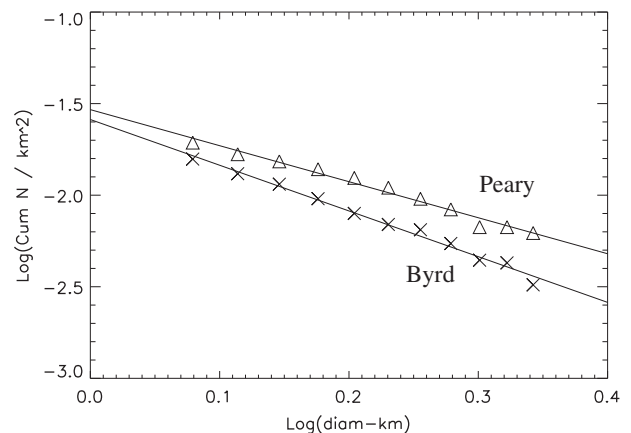


Fig. 15. Cumulative crater frequency plots for the floor deposits of Byrd and Peary craters, using the radar image data of Fig. 14A. The function slope is about -2 for Peary, and about -2.5 for Byrd, with the difference attributed to a cluster of Orientale secondary craters within Peary. The number density (rather than the cumulative count) of craters is almost identical for the two sample regions for craters smaller than about 2.5 km diameter.

for the south polar crater floors and some terra patches is not mirrored across the northern highlands. The depth of ejecta from the basin is predicted to be about three times thicker at the south pole than at the north pole, based on the scaling model of McGetchin et al. (1973), which may explain part of these differences. Whether thicker, melt-rich deposits are found in plains-like material on west-limb crater floors closer to Orientale (and thus more analogous to the 2300-km radial distance from the basin center to the south pole) must wait for more favorable northwest librations or orbital radar imaging.

5. Conclusions

The S-band campaign to map the lunar nearside is producing mosaicked data with well-calibrated CPR values, and is currently about half completed. Regional averaging of the data shows that circular polarization ratio values at 12.6-cm wavelength for low-to moderate-TiO₂ mare basalt deposits can exceed those of rough terrestrial lava flows. We attribute this difference to abundant few-centimeter diameter rocks from small impacts and a significant component of subsurface volume scattering. An outflow deposit inferred to be impact melt from Glushko crater has high CPR values at 12.6-cm and 70-cm wavelengths, and thus a very rugged near-surface structure at the decimeter to meter scale. This deposit does not show radar-brightness variations consistent with levees or channels, and appears to nearly overtop a massif, suggesting very rapid emplacement. Deposits of similar morphology and radar brightness are noted for craters such as Pythagoras, Rutherford, Theophilus, and Aristillus. Images of the north pole show that, despite recording the deposition of Orientale material, Byrd and Peary craters do not have dense patterns of radar-bright ejecta from small craters on their floors. Such patterns in Amundsen crater, near the south pole, were interpreted as diagnostic of abundant impact melt, so the fraction of Orientale-derived melt in the north polar smooth plains, 1000 km farther from the basin center, is inferred to be much lower.

Acknowledgments

We thank the staff at Arecibo Observatory and the Green Bank Telescope for their tremendous efforts in support of our radar mapping. The Arecibo Observatory is part of the National Astronomy and Ionosphere Center, which is operated by Cornell University under a cooperative agreement with the National Science Foundation (NSF). The Green Bank Telescope is part of the National Radio Astronomy Observatory, a facility of the NSF operated under cooperative agreement by Associated Universities, Inc. The lunar radar mapping is supported by a grant to B.A.C. from the NASA Planetary Astronomy Program. The comments of two anonymous reviewers helped to improve the manuscript.

References

- Black, G.J., Campbell, D.B., Nicholson, P.D., 2001. Icy Galilean satellites: Modeling radar reflectivities as a coherent backscatter effect. *Icarus* 151, 167–180.
- Campbell, B.A., 2009. Scale dependent surface roughness behavior and its impact on empirical models for radar backscatter. *IEEE Trans. Geosci. Rem. Sens.* 47, 3480–3488. doi:10.1109/TGRS.2009.2022752.
- Campbell, B.A., Campbell, D.B., 2006. Surface properties in the south polar region of the Moon from 70-cm radar polarimetry. *Icarus* 180, 1–7.
- Campbell, B.A., Bell, J.F., Zisk, S.H., Hawke, B.R., Horton, K.A., 1992. A high-resolution radar and CCD imaging study of crater rays in Mare Serenitatis and Mare Nectaris. *Proc. Lunar Sci. Conf. XXII*, 259–274.
- Campbell, B.A., Hawke, B.R., Thompson, T.W., 1997. Regolith composition and structure in the lunar maria: Results of long-wavelength radar studies. *J. Geophys. Res.* 102 (19), 19307–19320.
- Campbell, D.B., Campbell, B.A., Carter, L.M., Margot, J.L., Stacy, N.J.S., 2006. Lunar polar ice. No evidence for thick deposits at the south pole. *Nature* 443, 835–837.
- Campbell, B.A., Campbell, D.B., Margot, J.L., Ghent, R.R., Nolan, M., Chandler, J., Carter, L.M., Stacy, N.J.S., 2007. Focused 70-cm radar mapping of the Moon. *IEEE Trans. Geosci. Rem. Sens.* 45 (12), 4032–4042. doi:10.1109/TGRS.2007.906582.
- Campbell, B.A., Hawke, B.R., Campbell, D.B., 2009a. Surface morphology of domes in the Marius Hills and Mons Rumker regions of the Moon from Earth-based radar data. *J. Geophys. Res.*, E01001. doi:10.1029/2008JE003253.
- Campbell, B.A., Hawke, B.R., Carter, L.M., Ghent, R.R., Campbell, D.B., 2009b. Rugged lava flows on the Moon revealed by Earth-based radar. *Geophys. Res. Lett.* 36, L22201. doi:10.1029/2009GL041087.
- Carrier, W.D., Olhoeft, G.R., Mendell, W., 1991. *Physical Properties of the Lunar Surface*. Lunar Sourcebook. Cambridge Univ. Press, New York, pp. 475–594.
- Carter, L.M., Campbell, D.B., Campbell, B.A., 2004. Impact crater related surficial deposits on Venus: Multi-polarization radar observations with Arecibo. *J. Geophys. Res.* 109, E06009. doi:10.1029/2003JE002227.
- Carter, L.M., Campbell, D.B., Campbell, B.A., 2006. Volcanic deposits in shield fields and highland regions on Venus: Surface properties from radar polarimetry. *J. Geophys. Res.* 111. doi:10.1029/2005JE002519.
- Chadwick, D.J., Schaber, G.G., 1993. Impact crater outflows on Venus: Morphology and emplacement conditions. *J. Geophys. Res.* 98, 20891–20902.
- Charette, M.P., McCord, T.B., Pieters, C., Adams, J.B., 1974. Applications of remote spectral reflectance measurements to lunar geology classification and determination of titanium content of lunar soils. *J. Geophys. Res.* 79, 1605–1613.
- Gault, D.E., Wedekind, J.A., 1978. Experimental studies of oblique impact. *Proc. Lunar Sci. Conf.* 9, 3483–3875.
- Ghent, R.R., Campbell, B.A., Hawke, B.R., Campbell, D.B., 2008. Earth-based radar data reveal extended deposits of the Moon's Orientale basin. *Geology* 36, 343–346. doi:10.1130/G24325A.1.
- Gillis, J.J., Joliff, B.L., Elphic, R.C., 2003. A revised algorithm for calculating TiO₂ from Clementine UVVIS data: A synthesis of rock, soil, and remotely sensed TiO₂ concentrations. *J. Geophys. Res.* 108. doi:10.1029/2001JE001515.
- Hagfors, T., 1970. Remote probing of the Moon by infrared and microwave emissions and by radar. *Radio Sci.* 5, 189–227.
- Hawke, B.R., Head, J.W., 1977. Impact melt on lunar crater rims. In: Roddy, D.J., Pepin, R.O., Merrill, R.B. (Eds.), *Impact and Explosion Cratering*. Pergamon, New York, pp. 815–841.
- Heather, D.J., Dunkin, S.K., 2003. Geology and stratigraphy of King crater, lunar farside. *Icarus* 163, 307–329.
- Hiesinger, H., Jaumann, R., Neukum, G., Head, J.W., 2000. Ages of mare basalts on the lunar nearside. *J. Geophys. Res.* 105, 29239–29275.
- Howard, K.A., Wilshire, H.G., 1975. Flows of impact melt at lunar crater rims. *J. Res. US Geol. Survey* 3, 237–251.
- Johnson, J.R., Baker, V.R., 1994. Surface property variations in venusian fluidized ejecta blanket craters. *Icarus* 110, 33–70.
- Keihm, S.J., Langseth, M.G., 1975. Lunar microwave brightness temperature observations reevaluated in the light of Apollo program findings. *Icarus* 24, 211–230.
- Lucey, P.G., Blewett, D.T., Joliff, B.D., 2000. Lunar iron and titanium abundance algorithms based on final processing of Clementine ultraviolet–visible images. *J. Geophys. Res.* 105, 20297–20306. doi:10.1029/1999JE001117.
- Luchitta, B.K., 1978. Geologic map of the north side of the Moon. USGS Misc. Inv. Series I-1062.
- McGetchin, T.R., Settle, M., Head, J.W., 1973. Radial thickness variation in impact crater ejecta: Implications for lunar basin deposits. *Earth Planet. Sci. Lett.* 20, 226–236.
- Pettengill, G.H., Zisk, S.H., Thompson, T.W., 1974. The mapping of lunar radar scattering characteristics. *Moon* 10, 3–16.
- Schaber, G.G., Thompson, T.W., Zisk, S.H., 1975. Lava flows in Mare Imbrium: An evaluation of anomalously low Earth-based radar reflectivity. *Moon* 13, 395–423.
- Schultz, P.H., Mendell, W., 1978. Orbital infrared observations of lunar craters and possible implications for impact ejecta emplacement. *Proc. Lunar Sci. Conf.* 9, 2857–2883.
- Shorthill, R.W., 1973. Infrared atlas charts of the eclipsed Moon. *Earth Moon Planets* 7, 22–45.
- Stacy, N.J.S., 1993. High-resolution Synthetic Aperture Radar Observations of the Moon. Ph.D. Thesis, Cornell University, Ithaca, NY.
- Stacy, N.J.S., Campbell, D.B., Ford, P.G., 1997. Radar mapping of the lunar poles: A search for ice deposits. *Science* 276, 1527–1530.
- Thompson, T.W., 1978. High resolution lunar radar map at 7.5 m wavelength. *Icarus* 36, 174–188.
- Thompson, T.W., 1987. High-resolution lunar radar map at 70 cm wavelength. *Earth Moon Planets* 37, 59–70.
- Thompson, T.W., Dyce, R.B., 1966. Mapping of lunar radar reflectivity at 70 centimeters. *J. Geophys. Res.* 71, 4843–4853.
- Thompson, T.W., Pollack, J.B., Campbell, M.J., O'Leary, B.T., 1970. Radar maps of the Moon at 70-cm wavelength and their interpretation. *Radio Sci.* 5, 253–262.
- Zisk, S.H., Pettengill, G.H., Catuna, G.W., 1974. High-resolution radar maps of the lunar surface at 3.8-cm wavelength. *Moon* 10, 17–50.